Heritage Science

RESEARCH

Open Access

Microscopic weathering mechanisms of subflorescence and crust patterns in the Nankan Grotto, northern Sichuan, China

Xuening Zhang[1], Sixiang Ling[1,2*], Xiyong Wu[1,2] and Jiawen Xie[1]

Abstract

The mineralogy, geochemical mass balance, sulfur isotope, and micro-structure of the sandstone in the Nankan Grotto were analyzed to explore the weathering mechanisms of the subflorescence and crust patterns. The results revealed that the mineralogical compositions of the rock samples from the subflorescence and crust sites were quartz, feldspar, calcite, and clay minerals. The calcite content was much higher in the crust site than that in the subflorescence site. Based on the microscopic petrographic evidence, the crystallization stress of the thenardite and calcite and the swelling/shrinking stress of the clay minerals led to the detachment of the outer rock layer, after which subflorescence became visible on the newly exposed surface. Solution migration carried Ca^{2+} from the interior of the rock to the surface, where it combined with CO_3^{2-} and SO_4^{2-} to produce gypsum and calcite on the surface during the drying process, resulting in the formation of the crust. Therefore, the mineralogical composition (especially the calcite content) laid the foundation for the distinct development of the subflorescence and crust. In addition, the microstructure and external environment influenced the amount and location of salt crystallization, eventually leading to thenardite crystallizing within the rock in the subflorescence site while the gypsum precipitated on the surface as a crust. The sulfur isotope analysis revealed that the sulfur in the subflorescence and crust sites was most likely derived from detergents and from the combustion of oil and natural gas. Our research revealed the microscopic weathering mechanisms of the subflorescence and crust patterns in the Nankan Grotto, providing insights on salt weathering mechanisms for stone heritage sites around the world.

Keywords Sandstone grotto, Deterioration mechanism, Deterioration pattern, Salt weathering, Sulfur isotope

Introduction

Sandstone buildings and monuments are an important part of our world's cultural heritage [1]. They have been subjected to diverse degradation processes over long geological timescales under the combined influences of external factors, such as environmental, geological, and anthropogenic disturbances [2–5], and internal factors, such as petrography and sedimentology [6–8]. In addition, salt weathering is widely accepted as an important weathering mechanism causing severe decay in sandstone heritage sites, as has been repeatedly demonstrated by numerous case studies [9–12]. Salt damage often results in the formation of efflorescence or crust on the surface, or the formation of subflorescence below the surface. Efflorescence, crust, and subflorescence patterns induce discoloration, deformation, and even detachment of the stone materials [13, 14]. These processes have greatly damaged the artistic value of sandstone heritage sites. Therefore, it is of great significance to further

*Correspondence:
Sixiang Ling
lingsx@swjtu.edu.cn
[1] Faculty of Geosciences and Environmental Engineering, Southwest Jiaotong University, Chengdu 611756, Sichuan, People's Republic of China
[2] MOE Key Laboratory of High-speed Railway Engineering, Southwest Jiaotong University, Chengdu 610031, Sichuan, People's Republic of China

explore the salt weathering mechanism of sandstone heritage sites and to provide appropriate protection.

The mechanisms of salt transport and the consequent weathering patterns are controlled by the petrography of the sandstone and the dominant environmental conditions [15]. The petrographic characteristics of the sandstone determined the type of salt and its concentration [16]. At the same time, the environmental conditions (such as temperature and relative humidity) controlled the drying kinetics of the solution, which further determined whether the salts would crystallize at the surface as efflorescence/crust or inside the material as damaging subflorescence [10]. In addition, the development of stone decay can be affected by anthropogenic disturbances, especially since the industrial revolution. Mass industrial and agricultural wastewater and waste gas have been discharged into the natural environment, which provided large salt sources for the salt weathering in sandstone grottoes [17–19].

The Nankan Grotto was dug from a sandstone cliff in approximately 700 AD in Bazhong City, and has since suffered severe salt weathering over a long geological timescale. However, the salt weathering mechanisms of the sandstone in the Nankan Grotto are still unclear. We conducted a field investigation and collected rock blocks and salt crystals for mineralogical, major element, sulfur isotope, and micro-structure analyses. The main objectives of this study were (i) to elucidate the weathering mechanisms of the subflorescence and crust patterns in the Nankan Grotto; (ii) to investigate the possible sulfur sources of the salt weathering in the Nankan Grotto; and (iii) to investigate the petrographic and environmental influences leading to the differentiation of rock deterioration. The results of this study provide new insights that improve our knowledge of the salt weathering processes in sandstone grottoes.

Study site and sampling

The Nankan Grotto is located in Bazhong City, Sichuan Province (Fig. 1a). The Nankan Grotto was first carved during the Sui dynasty and was then further carved during the Tang dynasty. It is an excellent representation of Buddhist and Taoist grotto art, which was included in the third group of major historical and cultural sites protected at the national level by the State Council in 1988. The existing sandstone grottoes are clustered in the Giant Buddha Cave Area (Fig. 1b–d).

Bazhong City is characterized by a subtropical humid monsoon climate and is frequently subjected to the Asian monsoon. The average annual temperature is approximately 16 °C. The lowest average daily temperature of 6.1 °C is in January, and the highest temperature of 27.1 °C occurs in July (http://www.cnbz.gov.cn). There are approximately 12–15 high-temperature days per year, on which temperature extremes of > 35 °C occur. The temperature rarely drops below 0 °C in winter, except for on an average of 2 or 3 days per year. The maximum temperature variations in a single day are approximately 20 to 35 °C in summer and − 2 to 13 °C in winter. The mean annual precipitation is approximately 1117.2 mm in the Bazhong area. The annual relative humidity (RH) varies from 64 to 84%. The relative humidity is relatively low in spring, with an average daily humidity of below 70%. The relative humidity is relatively high in winter, and the

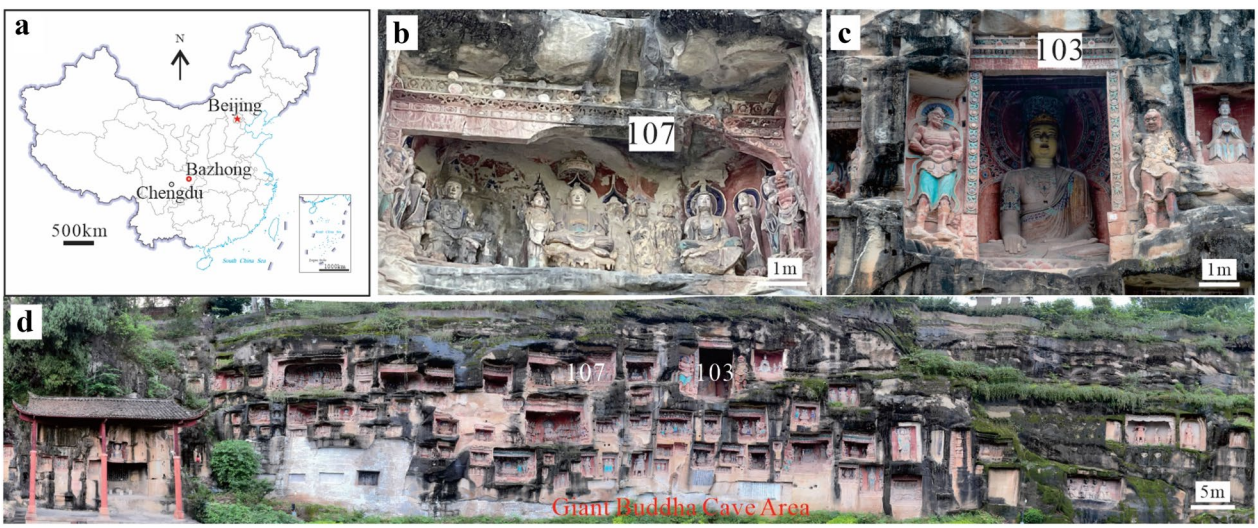

Fig. 1 **a** Location of the study area. **b** Photograph of Grotto 107. **c** Photograph of Grotto 103. **d** Field photograph of the Nankan Grotto. The Arabic numerals in b, c, and d are the sequential numbers of the Buddhas

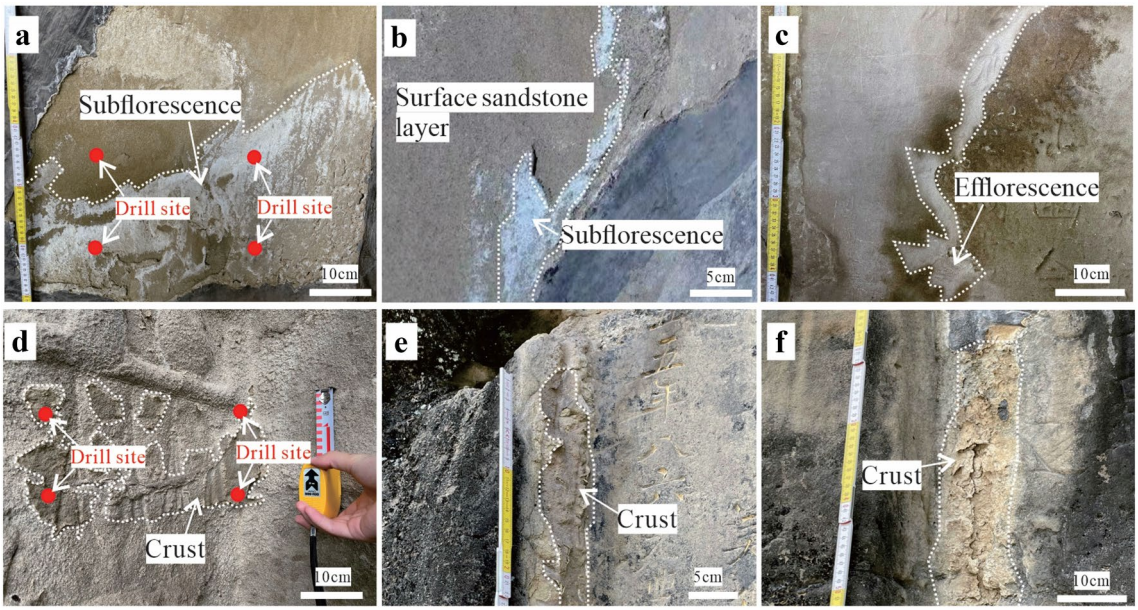

Fig. 2 Field observations and sampling sites of the different deterioration patterns in the Nankan Grotto. **a**, **b** Subflorescence site. **c** Efflorescence site. **d**–**f** Crust site. The red dots in a and d denote the drill sites

average relative humidity from October to December is greater than 80%. The maximum relative humidity variations on rainy days range from approximately 60–98%.

The sandstone, excavation material for the Nankan Grotto, has a reddish color and is from the Lower Cretaceous Bailong Formation. The salt weathering patterns in the Nankan Grotto can be mainly classified as subflorescence (Fig. 2a, b), efflorescence (Fig. 2c), and crust (Fig. 2d–f). The subflorescence and efflorescence are composed of white salt particles that poorly adhere on the sandstone surfaces or newly exposed surfaces (Fig. 2a–c), while the crust is hard and bonded to the stone surface. The crust is brown or dark brown and includes the products of extraneous sedimentary materials and secondary mineralization (Fig. 2d–f). Based on the Illustrated Glossary on Stone Deterioration Patterns established by the International Council on Monuments and Sites (ICOMOS) for stone [20], efflorescence and subflorescence can be distinguished as follows. Efflorescence is generally poorly bonded to the stone surface and is not suspected to cause severe damage to the material. Subflorescence corresponds to salt crystallization inside the material pores and under the stone surface. Subflorescence is also visible on the newly exposed surface when the stone layer over it has detached. Therefore, the damage caused by subflorescence is much more severe than that caused by efflorescence.

We collected three samples from a subflorescence site and three samples from a crust site to investigate their deterioration mechanisms. Samples S0, S1, and S2 were collected from the subflorescence site. Sample S0 was the white salt crystallization on the surface, while samples S1 and S2 were the weathered and fresh rock samples, respectively, from the subflorescence site (Fig. 2a). Samples C0, C1, and C2 were collected from the crust site. Sample C0 was the brown crust attached to the cliff surface, while samples C1 and C2 were the weathered and fresh rock samples, respectively, from the crust site (Fig. 2d). Salt crystal sample S0 was collected using a brush. Crust sample C0 was collected using a knife. Then, a microscopic drill (HZD-L, China) was used to drill horizontal micro holes with a diameter of 50 mm in the newly exposed sandstone surface. At the subflorescence and crust sites, four holes were drilled in each site, with a horizontal drilling depth of 10 cm (Fig. 2a, d). Each sampling site yielded two samples: the 0–3 cm depth sandstone cores were denoted as weathered sandstone samples (sample S1 or C1), and the 4–10 cm depth sandstone cores were denoted as fresh sandstone samples (sample S2 or C2). The weathering state of the sandstone core was classified based on the particle color, hardness, and fissures.

Methods

Mineralogical analysis

After the collection, the samples were completely dried in a drying oven at 60 °C until a constant mass was achieved. Then, the whole rock samples were pulverized to silt-sized particles using an agate mortar and pestle. Before the laboratory analyses, the crushed samples were

ground to 200 mesh (< 75 μm) powder using an XQM-0.4 A ball mill and a zirconia ball. The mineralogical compositions of the powdered whole rock samples were determined via X-ray diffraction (XRD) using Cu-Kα radiation (Bruker D8 DISCOVER, Germany; 40 kV; 40 mA; λ = 1.54059 Å). The whole rock samples were analyzed at 2θ angles of 5° to 45° and a step size of 0.02°/sec.

The clay fractions (< 2 μm) were separated from the bulk sandstone powder using a previously published method [21, 22]. First, the powdered samples were dissolved in 20% diluted acetic acid to remove the carbonate components. They were allowed to settle for approximately 60 h. Then, the uppermost suspension was transferred to a polyethylene tube and centrifuged at 2000 rpm for 5 min to settle the clay fraction. The clay fraction was collected and suspended in distilled water, and then it was sonicated to achieve dispersion. Finally, this clay suspension was pipetted onto a glass slide and dried at room temperature for 48 h. The clay fractions were further treated via (i) air drying, (ii) the addition of ethylene glycol, and (iii) thermal-processing at 450 °C. All of the treated clay samples on the glass slides were then analyzed using XRD at 2θ angles of 2.5° to 15° and a step size of 0.02°/sec. The mineral contents were quantified using whole pattern fitting and Rietveld refinement. The relative standard deviation (RSD) of the XRD measurements was less than 10%. The lowest detection limit was 0.1 wt.%.

Major element analysis

The major element compositions were analyzed via X-ray fluorescence spectroscopy (XRF; PANalytical PW2424, Netherlands). For the chemical analysis, two portions of each powdered samples were weighed out. One sample was fused with $LiBO_2$-$Li_2B_4O_7$ flux and an oxidizing agent ($LiNO_3$). Then, the melted sample was poured into a platinum mold and prepared for XRF analysis. Another sample was calcined in a muffle furnace with oxygen at 1000 °C to calculate the loss on ignition (LOI). Measurements were carried out on standard and parallel samples, and the relative deviation (RD) and relative error (RE) of the XRF measurements were less than 5%. The lowest detection limit was 0.01 wt%.

Pore measurement

The pore size distribution was determined using mercury intrusion porosimetry (MIP, Micromeritics AutoPore IV 9505, America). Before measurements were taken, the rock samples were crushed into centimeter sized fragments and heated at 105 °C for 24 h under high vacuum conditions. Then, the pore volume was measured via the intrusion of mercury at discrete pressure steps until the maximum pressure of 110 MPa was reached.

Sulfur ($\delta^{34}S$) isotope analysis

Sulfur ($\delta^{34}S$) isotope analyses were conducted on the six samples to trace the possible sources of the sulfur. First, the sulfur was separated from the matrix and precipitated as $BaSO_4$. The sulfur isotopic composition was measured using a stable isotope ratio mass spectrometer (Finnigan MAT 253, Germany) coupled to an elemental analyzer (Costech ECS 4010, Italy). The $\delta^{34}S$ values were calculated by normalizing the $^{34}S/^{32}S$ ratio of the sample to that of the Vienna Canyon Diablo Troilite (VCDT) international standard. The relative standard deviation (RSD) of the measurements was less than 0.03%. The lowest detection limit was 0.1‰. The analytical precision for the $\delta^{34}S$ value was reproducible to 0.2‰.

Microscopic petrographic analysis

The unpolished samples (S0 and C0) were coated with platinum (Emitech SC7620 sputter coater) prior to observation. The microstructures of samples S0 and C0 were observed using a field emission scanning electron microscope (FE-SEM; TESCAN MIRA 3, Czech Republic). Before the observations, sandstone samples S1, S2, C1, and C2 were polished using a polishing machine (UNIPOL-1200 M) to obtain flat surfaces. Then, backscattered electron (BSE) images of samples S1, S2, C1, and C2 were obtained via FE-SEM. The instrument was operated at an accelerating voltage of 20 kV. The element compositions of the observed grains were analyzed via energy dispersive X-ray spectroscopy (EDS; EDAX Element 30).

Results

Mineralogy of the sandstone

The XRD analysis results of the samples are shown in Table 1 and Fig. 3. For the subflorescence samples (S0, S1, and S2), the quartz contents (60.7–79.4 wt.%) were the highest, and the calcite contents (0.5–9.2 wt.%) were the lowest. The other minerals were feldspar (13.3–14.6 wt.%) and clay mineral (4.5–8.5 wt.%). Thenardite was only observed in sample S0 in this set of samples (8.3 wt.%). For the clay minerals, the illite-smectite mixed layer contents were the highest (2.1–2.9 wt.%), followed by the mica/illite contents (1.4–2.1 wt.%). The chlorite contents (0.3–0.5 wt.%) and kaolinite contents (0.2–0.5 wt.%) were much lower.

The crust samples (C0, C1, and C2) had the highest quartz contents (64.1–74.1 wt.%), followed by the feldspar (10.3–15.0 wt.%), calcite (6.1–15.1 wt.%), and clay mineral (5.4–8.2 wt.%) contents. Gypsum was only observed in samples C0 and C1 (1.3–2.3 wt.%). For the clay minerals, the illite-smectite mixed layer contents were the highest (3.4–6.0 wt.%), followed by the mica/illite (0.6–1.3 wt.%), chlorite (0.3–0.4 wt.%), and kaolinite (0.4 wt.%) contents. The calcite and illite-smectite mixed

Table 1 Mineral contents (wt.%) of the samples by XRD.

Deterioration pattern	Sample	Weathering State	Qz	Fsp	Cal	Gp	Thn	Clay minerals				
								Total	Ilt-Sme	Mca/Ilt	Chl	Kln
Subflorescence	S0	Salt crystals	60.7	13.3	9.2	-	8.3	8.5	/	/	/	/
	S1	Weathered	79.4	13.8	0.5	-	-	5.4	2.9	2.1	0.3	0.2
	S2	Fresh	78.9	14.6	2.0	-	-	4.5	2.1	1.4	0.5	0.5
Crust	C0	Salt crystals	64.1	10.3	15.1	2.3	-	8.2	/	/	/	/
	C1	Weathered	67.6	15.0	8.7	1.3	-	7.4	6.0	0.6	0.4	0.4
	C2	Fresh	74.1	14.4	6.1	-	-	5.4	3.4	1.3	0.3	0.4

Qz = quartz, Fsp = feldspar, Cal = calcite, Gp = gypsum, Thn = thenardite, Ilt-Sme = illite-smectite mixed layer, Mca/Ilt = mica/illite, Kln = kaolinite, Chl = chlorite

- indicates that the concentration is below detection limit (0.1 wt%); / denotes not analyzed

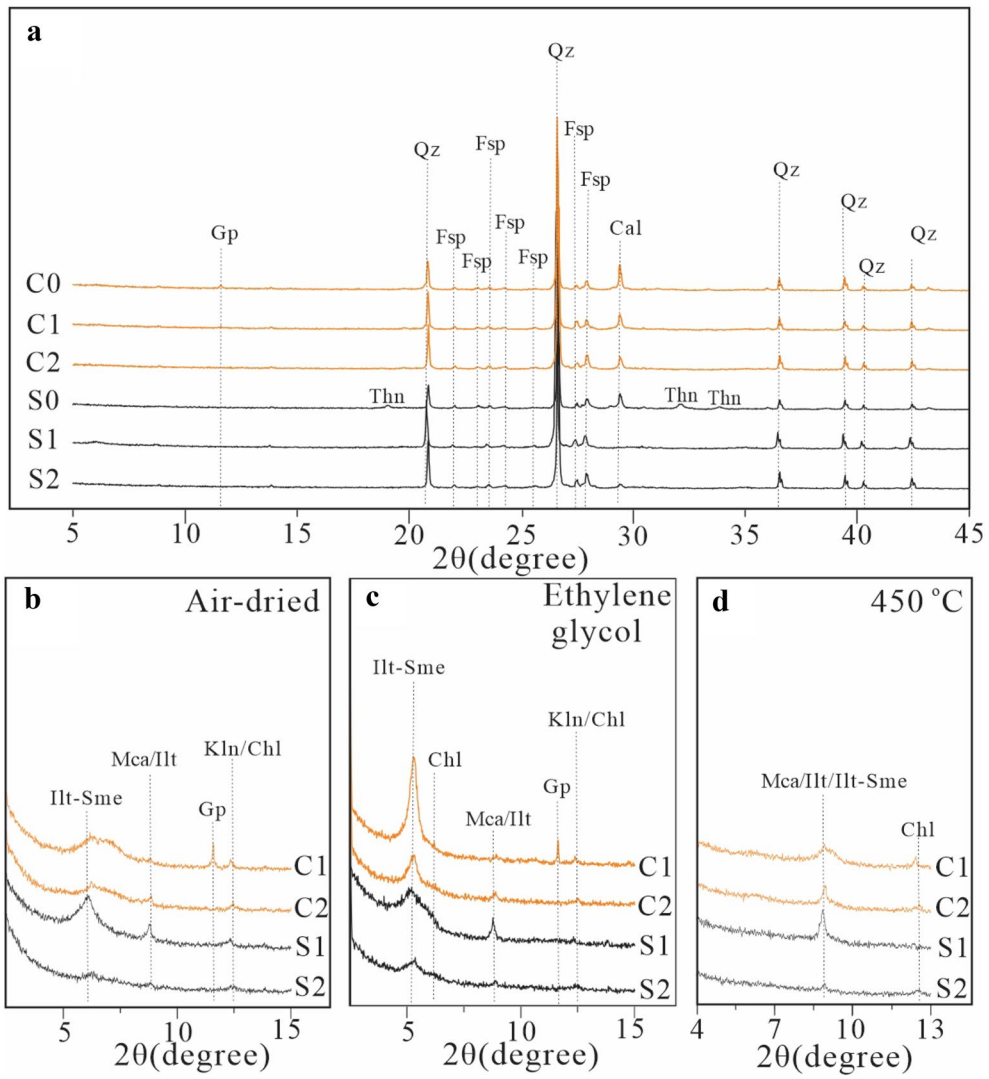

Fig. 3 X-ray diffraction mineral analysis results for the rock samples. **a** Whole rock sample. **b** Air-dried condition for clay fractions. **c** Ethylene glycol treatment for clay fractions. **d** Thermal treatment for clay fractions. The mineral symbols are the same as in Table 1

Table 2 Major element compositions (%) of the samples from the different sites

Deterioration pattern	Sample	SiO_2	Al_2O_3	CaO	TFe_2O_3	K_2O	Na_2O	MgO	MnO	P_2O_5	SO_3	TiO_2	LOI
Subflorescence	S1	81.30	8.18	0.70	3.01	1.86	1.48	0.81	0.04	0.07	0.01	0.41	1.71
	S2	80.53	7.95	2.27	1.72	1.69	1.62	0.92	0.04	0.05	0.03	0.43	2.82
Crust	C1	74.72	7.63	5.73	1.21	1.70	1.59	0.93	0.04	0.04	1.88	0.23	5.96
	C2	76.47	7.52	5.34	1.06	1.71	1.48	0.75	0.04	0.05	0.01	0.20	5.24

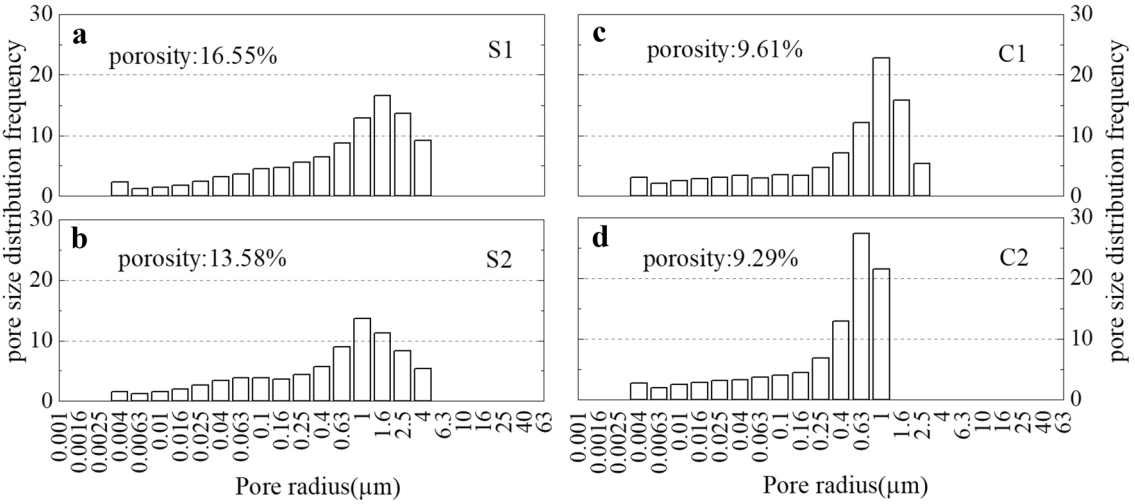

Fig. 4 Porosity and pore size distribution frequency results of the rock samples. **a** Porosity and pore size distribution frequency of sample S1. **b** Porosity and pore size distribution frequency of sample S2. **c** Porosity and pore size distribution frequency of sample C1. **d** Porosity and pore size distribution frequency of sample C2. Samples S0 and C0 were too fragmented to conduct porosity measurements on

layer contents of rock samples C1 and C2 were much higher than those of samples S1 and S2.

Major element compositions

The major element compositions are summarized in Table 2. For the subflorescence samples (S1, S2), the SiO_2 contents (80.53–81.30%) were the highest, followed by the Al_2O_3 (7.95–8.18%), Fe_2O_3 (1.72–3.01%), CaO (0.70–2.27%), K_2O (1.69–1.86%), Na_2O (1.48–1.62%), and MgO (0.81–0.92%) contents. Sample S1 had the highest SiO_2 content (81.30%) and the lowest CaO content (0.70%), corresponding to the abundance of the quartz and the sparsity of the calcite. The contents of the other oxides, such as MnO (0.04%), P_2O_5 (0.05–0.07%), SO_3 (0.01–0.03%), and TiO_2 (0.41–0.43%), were all less than 1.0%.

For the crust samples (C1, C2), the major element oxide contents were as follows: SiO_2 (74.72–76.47%), Al_2O_3 (7.52–7.63%), CaO (5.34–5.73%), K_2O (1.70–1.71%), Na_2O (1.48–1.59%), Fe_2O_3 (1.06–1.21%), and MgO (0.75–0.93%). Sample C1 had the highest SO_3 content of all of the samples (1.88%), as a result of the precipitation of gypsum. The MnO (0.04%), P_2O_5 (0.04–0.05%), and TiO_2 (0.20–0.23%) contents were less than 1.0%.

Porosity

The porosity and pore size distribution frequency results are shown in Fig. 4. At the subflorescence site, the porosity increased from sample S2 to sample S1 (from 13.58% to 16.55%). At the crust site, the porosity showed less variation from sample C2 to sample C1 (from 9.29% to 9.61%). In general, the porosities and the proportions of macropores (> 1 μm) at the subflorescence site were much higher than those at the crust site.

Sulfur ($\delta^{34}S$) isotope analysis

The sulfur ($\delta^{34}S$) isotope results of samples S0, C0, and C1 from the Nankan Grotto are shown in Table 3. The sulfur contents of samples S1, S2, and C2 were too low to conduct sulfur ($\delta^{34}S$) isotope analysis. The $\delta^{34}S$ values of samples S0, C0, and C1 were +14.9‰, +10.0‰, and +8.8‰, respectively.

Table 3 Sulfur ($\delta^{34}S$, ‰) isotope analysis results for the samples from the Nankan Grotto

Deterioration pattern	Sample	$\delta^{34}S$ (‰)
Subflorescence	S0	14.9
	S1	-
	S2	-
Crust	C0	10.0
	C1	8.8
	C2	-

- indicates below the detection limit (0.1‰)

Microscopic observations

In the subflorescence site, the quartz and feldspar surfaces were smooth in fresh sandstone sample S2 and the micro-structures of the minerals were intact (Fig. 5). The cement was mainly composed of siliceous materials. As the weathering progressed, the matrix was significantly dissolved in weathered sample S1. Sample S1 exhibited a more porous structure with looser contacts and less cementation between adjacent particles. Obvious microcracks had developed in the quartz and feldspar, making them more fragmented. Chlorite was observed on the edges of the feldspar, exhibiting an acicular texture.

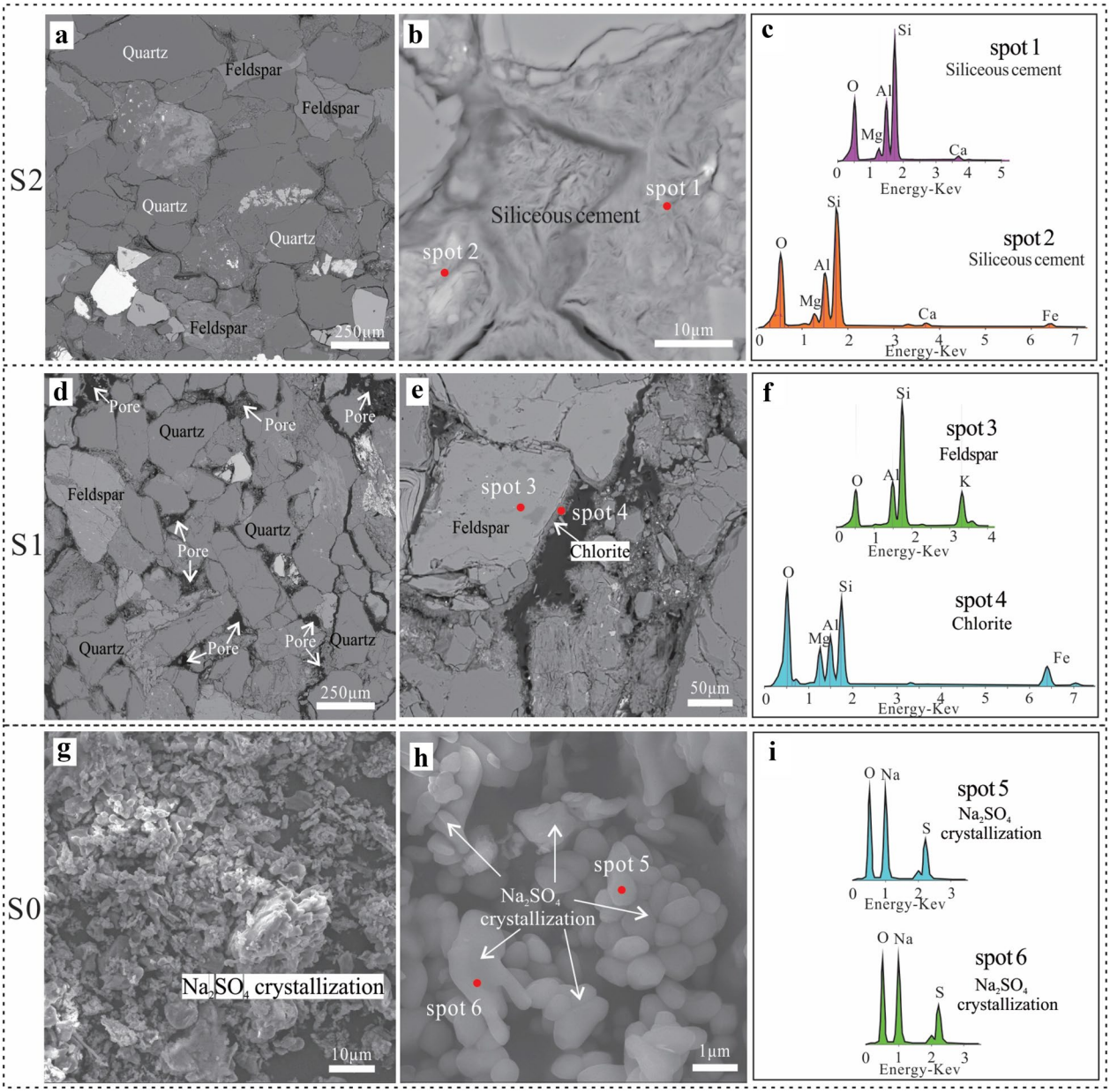

Fig. 5 SEM and BSE micrographs and representative EDS spectra of the samples from the subflorescence site. **a**–**c** BSE images and EDS spectra of sample S2. **d**–**f** BSE images and EDS spectra of sample S1. **g**–**i** SEM images and EDS spectra of sample S0

In salt crystal sample S0, clusters of spherical crystals of thenardite had precipitated on the mineral surfaces in a cauliflower-like shape.

The calcite contents of samples C1 and C2 from the crust site were much higher than those of samples S1 and S2 from the subflorescence site, which was consistent with the XRD results (Fig. 6). In fresh sample C2, the surfaces of the mineral grains were flat and well-bonded, so the micro-structures of the minerals were intact. The cement material in sample C2 was mainly composed of siliceous materials. Calcite was widely observed in the gaps between the minerals. As weathering proceeded, the mineral grains were loosely scattered, and trans-crystalline cracks were widely developed in the calcite and feldspar in weathered sandstone sample C1. The feldspar grains were severely altered, with densely distributed dissolution grooves and sericitization of the feldspar surfaces. In crust sample C0, the euhedral gypsum crystals exhibited tabular or clubbed shapes and were attached to the mineral surfaces.

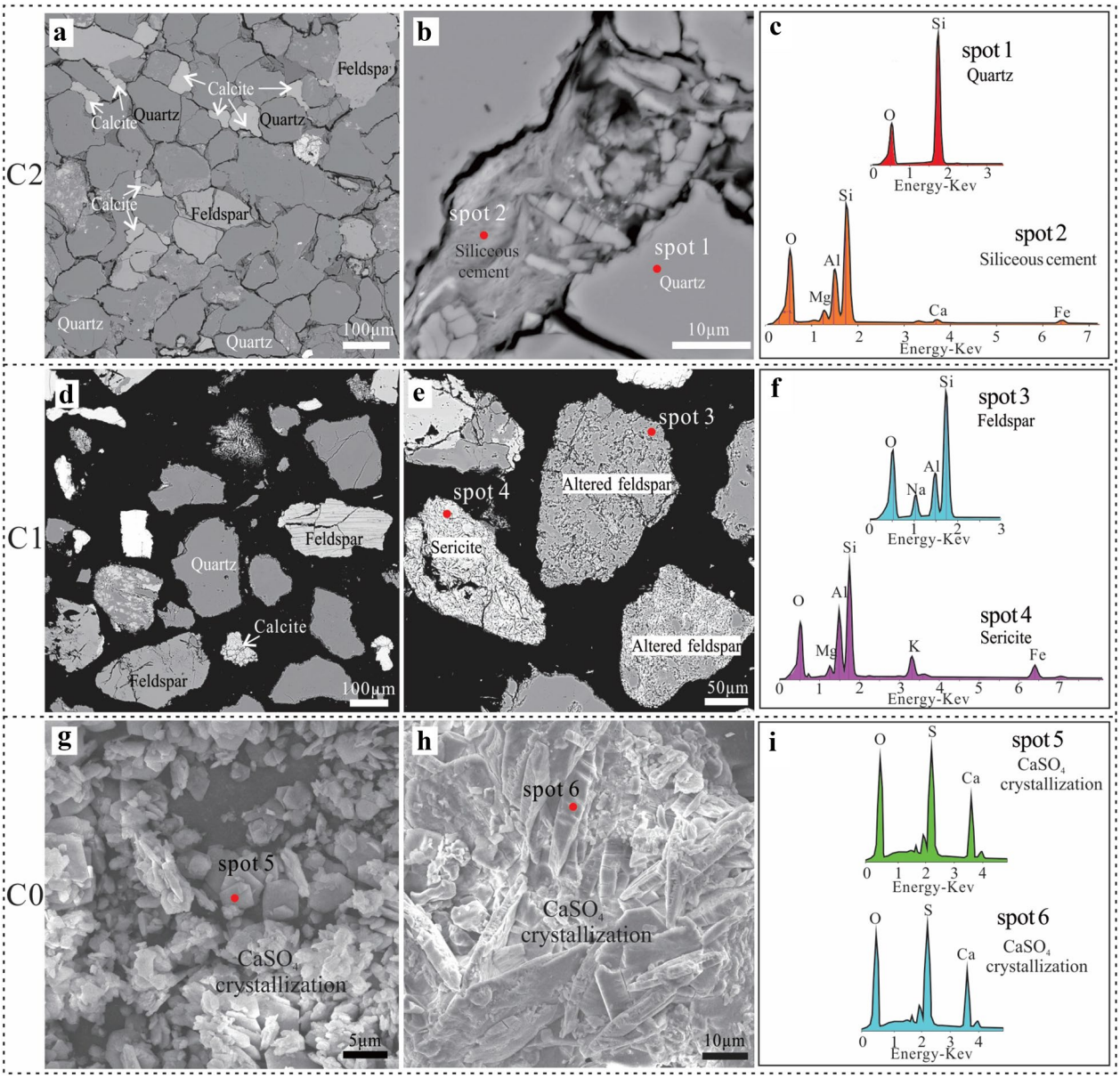

Fig. 6 SEM and BSE micrographs and representative EDS spectra of the samples from the crust site. **a**–**c** BSE images and EDS spectra of sample C2. (d–f) BSE images and EDS spectra of sample C1. **g**–**i** SEM images and EDS spectra of sample C0

Discussion

Microscopic weathering mechanism of the subflorescence

Based on the mineralogical analyses (Table 1) and microscopic observations (Fig. 5), the development of the subflorescence was likely related to the salt crystallization. Compared to fresh rock sample S2, sample S0 had the highest calcite content in the subflorescence site (9.2 wt.%; Table 1), indicating that its calcite was a secondary precipitate. The calcite crystallization stress was sufficient to split the quartz grains and exceed the overburden load [23, 24]. Sample S0 also had a high thenardite (Na_2SO_4) content (8.3 wt.%; Table 1), which was also visible in the microscopic observations (Fig. 5g–h). This indicated that thenardite crystallized in the subflorescence site. There are two stable phases in the Na_2SO_4-H_2O system: thenardite (Na_2SO_4) and mirabilite ($Na_2SO_4{\cdot}10H_2O$). Thenardite (Na_2SO_4) has been reported to precipitate directly from a solution at a temperature of > 32.4 °C, and it dissolves at a relative humidity of > 70% (20 °C). Below this temperature, the stable phase is mirabilite ($Na_2SO_4{\cdot}10H_2O$), and mirabilite rapidly dehydrates to thenardite at a relative humidity (RH) of < 71% (20 °C) [25–27]. Long-term changes in the temperature and relative humidity can lead to dissolution-crystallization cycles between mirabilite and thenardite. The precipitation of mirabilite or thenardite from a supersaturated solution would exert a large crystallization stress, which could exceed the tensile strength of sandstone [28]. Samples S2 and S1 had higher porosities and proportions of macropores (> 1 μm) (Fig. 4), which provided convenient channels for solution transportation and important sinks for salt precipitation. The cations (e.g., Ca^{2+} and Na^{+}) and anions (e.g., CO_3^{2-}) that formed calcite and mirabilite/thenardite were released from the weathering of primary minerals: Ca^{2+} and CO_3^{2-} were released from the dissolution of calcite, and the weathering of albite and plagioclase to sericite or other clay minerals released Na^{+} and Ca^{2+} into the solution [29]. The SO_4^{2-} in the solution was exogenous, as discussed in Sect. Possible sulfur sources for subflorescence and crust in the Nankan Grotto.

In addition, the clay mineral contents (mainly illite-smectite mixed layer and mica/illite) increased from sample S2 to sample S0 (Table 1), because of the weathering of the feldspar. Chlorite was also observed attached to the feldspar edges (Fig. 5e). The swelling clay minerals inflicted strong swelling/shrinking stress on the mineral boundaries, further widening the previously formed microcracks when they were hydrated and dehydrated [30, 31]. The crystallization stress of sodium sulfate and calcium carbonate was the main cause of the detachment of the outer rock layer, and the swelling/shrinking stress of the clay minerals was a secondary cause. As a result, subflorescence became visible on the newly exposed rock surface. The microscopic weathering mechanism of the subflorescence is shown in Fig. 7, and the development stages can be summarized as follows.

Stage I (Fig. 7a): The initial rock mass was fresh and complete, with no fissures. Water or vapor penetrated into the superficial rock, and then evaporation occurred, creating an area (a few centimeters deep) that repeatedly suffered dry-wet cycles.

Stage II (Fig. 7b): As the weathering proceeded, the weathering of the calcite and feldspar released cations (e.g., Ca^{2+}, Na^{+}) and anions (e.g., CO_3^{2-}) into the

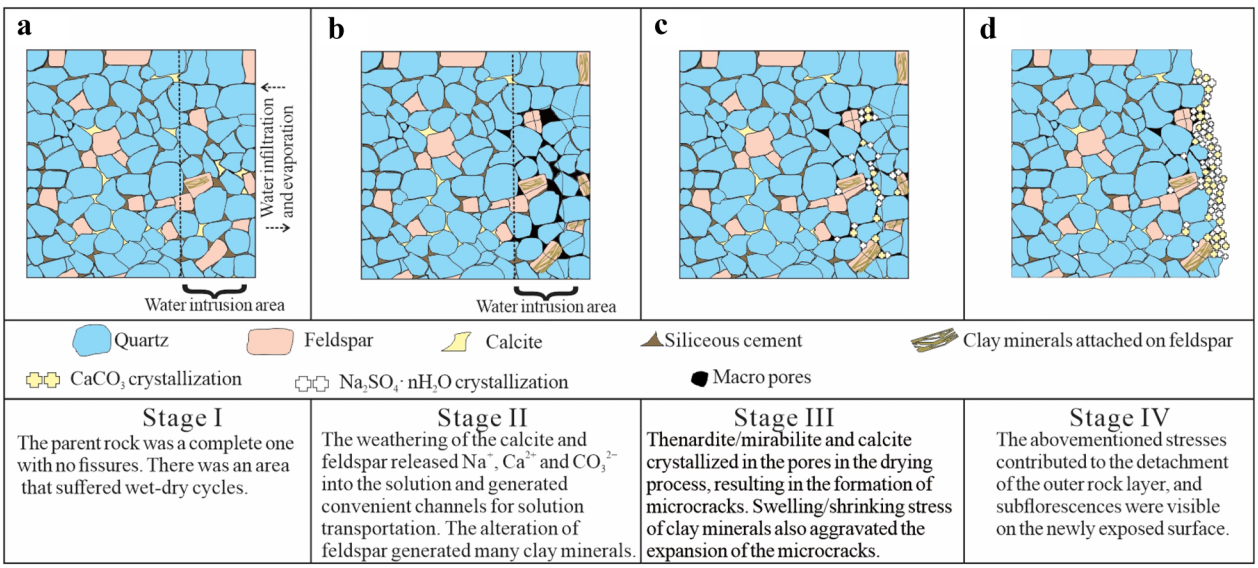

Fig. 7 Schematic diagram of the weathering processes of the subflorescence in the Nankan Grotto. **a** Stage I. **b** Stage II. **c** Stage III. **d** Stage IV

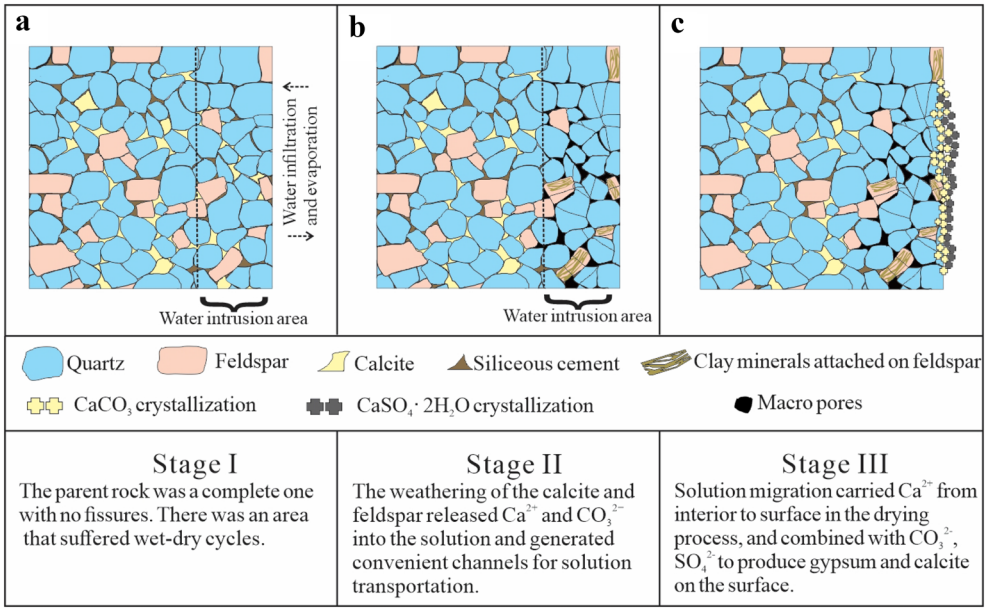

Fig. 8 Schematic diagram of the weathering processes of the crust in the Nankan Grotto. **a** Stage I. **b** Stage II. **c** Stage III

solution [29]. There was also some SO_4^{2-} in the solution. The dissolution of the calcite and feldspar generated convenient channels for solution transportation. In addition, the alteration of the feldspar generated many clay minerals attached to the feldspar surfaces.

Stage III (Fig. 7c): During the evaporation process, thenardite/mirabilite and calcite crystallized in the pore spaces and inflicted crystallization stress, resulting in the formation of microcracks in the rock mass. Swelling/shrinking stress was created by the hydration/dehydration of the clay minerals, which aggravated the expansion of the microcracks.

Stage IV (Fig. 7d): The abovementioned stresses contributed to the detachment of the outer rock layer, and subflorescence was visible on the newly exposed rock surface.

Microscopic weathering mechanism of the crust

In the crust site, gypsum was detected in samples C0 and C1 (Table 1) and was observed in sample C0 (Fig. 6g, h). Calcium sulfate generally occurs as anhydrite ($CaSO_4$) under unsaturated solution conditions, and it is hydrated to gypsum ($CaSO_4{\cdot}2H_2O$), which is accompanied by increased volume and hardening [32, 33]. Compared to the calcite content of fresh rock sample C2, sample C0 exhibited the highest calcite content (15.1 wt.%; Table 1), suggesting that secondary calcite was re-precipitated in the crust. The calcite generally coexisted with the gypsum, as an intermediate layer between the surface gypsum and the host rock [2]. Ca^{2+} and CO_3^{2-} were released from the dissolution of calcite, and the weathering of plagioclase also released Ca^{2+} into the solution [29]. The precipitation of calcite and gypsum on the rock surfaces led to the formation of the crust. The microscopic weathering mechanism of the crust is shown in Fig. 8, and the development stages can be summarized as follows.

Stage I (Fig. 8a): The initial rock mass was fresh and complete. The rock surface was subjected to frequent dry-wet cycles because of water or vapor penetration and evaporation.

Stage II (Fig. 8b): As weathering proceeded, the weathering of the calcite and feldspar released Ca^{2+} and CO_3^{2-} into the solution [29]. There was also some SO_4^{2-} in the solution. The dissolution of the calcite generated convenient channels for solution transportation.

Stage III (Fig. 8c): The Ca^{2+} migrated from the interior toward the outside of the sandstone during the drying process, and it combined with CO_3^{2-} and SO_4^{2-} to produce calcite and gypsum on the sandstone surfaces.

Possible sulfur sources for subflorescence and crust in the Nankan Grotto

The sulfur contents of fresh samples S2 and C2 were too low to conduct sulfur ($\delta^{34}S$) isotope analysis. Therefore, the sulfur in the subflorescence and crust was exogenous. There are three main sources of exogenous sulfur: regionally-transported sulfur (such as sea salt sulfur), natural biogenic sulfur, and anthropogenic sulfur. The $\delta^{34}S$ of sea salt sulfur is +21.0‰ [34]. The contents of the S species originating from sea salts were consistently very

low because the Sichuan Basin is located approximately 700 km inland from the coast of China [35]. Biogenic sulfur can be supplied by marine and terrestrial sources, and it is mainly released in the forms of H_2S and dimethylsulfur (DMS). Biogenic sulfur released from soils and wetlands was depleted in ^{34}S [36]. The $\delta^{34}S$ values of the biogenic sulfur reported in southern China have a narrow range of −3.0 to −2.0‰ [37]. Therefore, sea salt sulfur and biogenic sulfur were not possible S sources for the subflorescence and crust in the Nankan Grotto.

Anthropogenic emissions of sulfur from industrial and consumer processes generally exhibit a wide range of $\delta^{34}S$ values depending on the sources (coal, oil, or gas). In southern China, coals usually have low $\delta^{34}S$ values [37]. Coal has been reported to have a $\delta^{34}S$ range of −6.1 to +7.4‰ in the Sichuan Basin [38]. In contrast, crude oil sampled from the four largest Chinese oil fields had higher $\delta^{34}S$ values, ranging from +7.2 to +24.2‰ [39, 40]. The natural gas in Sichuan Basin had a high H_2S content, and its $\delta^{34}S$ value was about +17.4‰ [41]. The $\delta^{34}S$ values of samples C1, C0, and S0 are within the $\delta^{34}S$ value ranges of oil and natural gas. The sulfur contained in chemicals can also be classified as anthropogenic sulfur. The $\delta^{34}S$ values of the fertilizers utilized in the Sichuan Basin were between −5.6 and +7.7‰ [38], which are lower than the $\delta^{34}S$ values of samples C1, C0, and S0. The $\delta^{34}S$ range of detergent was characterized by rather high $\delta^{34}S$ values of +15.2 to +17.2‰ [38], which are consistent with the $\delta^{34}S$ value of sample S0. There are many residents living on the Nankan mountainside, and their waste water, which contains detergent, was discharged directly into the groundwater. Therefore, the thenardite formed in the subflorescence site and the gypsum formed in the crust site were most likely derived from the soluble SO_4^{2-} from detergents and the combustion of oil and natural gas.

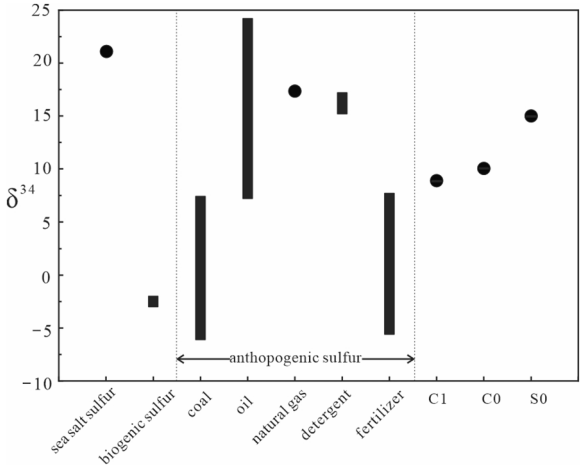

Fig. 9 The $\delta^{34}S$ values of the samples from the Nankan Grotto and from references

Petrographic and environmental influences on the differential development of the subflorescence and crust

At the subflorescence site, the salts were thenardite and secondary calcite, which were secondary precipitates in the interior pores or fissures in the sandstone. At the crust site, the salts were gypsum and secondary calcite, which were secondary precipitates on the rock surface. What is the reason for such a difference? The authentic calcite content in the crust site was much higher than that in the subflorescence site (Table 1), providing more Ca^{2+} to preferentially form gypsum in the crust site. Previous studies have shown that thenardite generally crystallizes within pores [25], while gypsum generally precipitates on surfaces [10]. This contrasting behavior of the two sulfates can be explained by considering the differences in the flow dynamics of solutions within porous materials [42]. The solubilities of calcium sulfate and sodium sulfate at 25 °C are 0.21 g and 27.9 g in 100 g of distilled water, respectively [43]. This means that the saturated sodium sulfate solution had a higher viscosity than the calcium sulfate solution. Therefore, the calcium sulfate solution had a higher flow rate in the pores and reached the stone surface faster to precipitate gypsum. However, the saturated sodium sulfate solution might precipitate mirabilite or thenardite in the pores before it reaches the stone surface during evaporation.

When the solution transports one salt through a pore system, the salt might accumulate beneath the stone surface when the pores are small. However, the petrographic characteristics of the subflorescence and crust sites demonstrated that there were two different salt solutions at each site: a sodium sulfate solution was present in the pores of the subflorescence site, while a calcium sulfate solution was present in the pores of the crust site. Samples S2 and S1 had higher porosities and greater proportions of macropores (>1 μm) than samples C2 and C1 (Fig. 4). Even though the microstructures were important in controlling the transport of salt solutions and the location of subsequent salt crystallization, the different physical properties of the calcium sulfate and sodium sulfate solutions at each site had crucial influences on the dynamics of the solution migration and evaporation, which resulted in thenardite crystallizing within the pores [25], while gypsum precipitated on the surface [10]. In addition, the macropores in the subflorescence site provided convenient channels for solution movement and important sinks for salt precipitation. In conclusion, the higher authentic calcite content in the crust site compared to the subflorescence site determined that gypsum ($CaSO_4{\cdot}2H_2O$) precipitated in the crust site whereas

mirabilite/thenardite ($Na_2SO_4 \cdot 10H_2O$/ Na_2SO_4) precipitated in the subflorescence site.

In addition, the environments (i.e., the temperature, relative humidity, and airflow) of the subflorescence and crust sites determined the evaporation rates, which further influenced the super-saturation degree of the salt solution and the crystal growth rate [16]. The microenvironment in the Nankan Grotto might have influenced the distinct development of the subflorescence and crust patterns. Long-term microenvironmental monitoring will be conducted at the two sampling sites to adequately elucidate the influences of the environment on the different sandstone deterioration patterns. Therefore, the different petrographies, microstructures, and outside environments led to the differences in the types, amounts, and locations of the salt crystallization, thus jointly controlling the thenardite crystallization within the pores in the subflorescence site and the gypsum precipitation on the surface in the crust site.

Conclusions

Mineralogical, major element, sulfur isotope, and microstructure analyses were conducted on samples of the sandstone in the Nankan Grotto. The main conclusions are as follows.

(1) The mineralogical compositions of the samples from the subflorescence and crust sites were quartz, feldspar, calcite, and clay minerals. The calcite content in the crust site was much higher than that in the subflorescence site. The porosities and the proportions of macropores (>1 μm) at the subflorescence site were much higher than those at the crust site.

(2) According to the mineralogical and microscopic petrographic analyses, thenardite and calcite crystallized inside the rock, resulting in the formation of the subflorescence. The precipitation of gypsum and calcite on the surface resulted in the formation of the crust.

(3) The sulfur isotope analysis revealed that the sulfur in the subflorescence and crust sites was most likely derived from anthropogenic sulfur, such as detergents and the combustion of oil and natural gas.

(4) The differences in the mineralogy (especially the calcite content) of the sandstone laid the foundation for the distinct development of subflorescence and crust patterns. The different physical properties of the calcium sulfate and sodium sulfate solutions had crucial influences on the dynamics of the crystallization of these salts. In addition, the microstructure and environment influenced the thermodynamic conditions of the solutions. These factors ultimately leaded to the distinct development of subflorescence and crust patterns. This research revealed the microscopic weathering mechanism of the subflorescence and crust patterns from various perspectives, which provides a foundation for further investigation into the salt weathering mechanisms of stone heritage sites around the world.

Acknowledgements
We greatly appreciate the field assistance and sample handling provided by Shiming Wang and Qiang Teng from Southwest Jiaotong University. We also would like to thank the colleagues of the Nankan Grotto Research Institute for their supports during field investigations.

Author contributions
Xuening Zhang wrote the main manuscript text and prepared Figs. 3, 4, 5, 6, 7 and 8. Sixiang Ling reviewed and edited the manuscript critically. Xiyong Wu prepared Figs. 1 and 2. Jiawen Xie prepared Fig. 9. All authors contributed to the research strategy, the discussion and interpretation of the results, and the final form of the text and figures. All authors read and approved the final manuscript.

Funding
This study was funded by the National Natural Science Foundation of China (No. 42077271, 42377198), National Cultural Heritage Administration of China (No. 2020ZCK110), Sichuan Science and Technology Program (No. 2023YFS0364), Chengdu Science and Technology Program (2022-YF05-00240-SN).

Availability of data and materials
The datasets used and/or analyzed during the current study are available from the corresponding author upon reasonable request.

Declarations

Ethics approval and consent to participate
Not applicable.

Consent for publication
Not applicable.

Competing interests
The authors declare no competing interests.

Received: 11 May 2023 Accepted: 19 August 2023
Published online: 29 August 2023

References

1. Fitzner B, Heinrichs K. Damage diagnosis on stone monuments–weathering forms, damage categories and damage indices. Acta-Universitatis Carol Geologica. 2001;1:12.
2. Germinario L, Oguchi CT, Tamura Y, Ahn S, Ogawa M. Taya Caves, a buddhist marvel hidden in underground Japan: stone properties, deterioration, and environmental setting. Herit Sci. 2020;8(1):87.
3. Liu XB, Koestler RJ, Warscheid T, Katayama Y, Gu JD. Microbial deterioration and sustainable conservation of stone monuments and buildings. Nat Sustain. 2020;3(12):991–1004.

4. Ortega-Morales O, Montero-Muñoz JL, Neto JAB, Beech IB, Sunner J, Gaylarde C. Deterioration and microbial colonization of cultural heritage stone buildings in polluted and unpolluted tropical and subtropical climates: a meta-analysis. Int Biodeterior Biodegrad. 2019;143:104734.
5. Rihosek J, Bruthans J, Masin D, Filippi M, Carling GT, Schweigstillova J. Gravity-induced stress as a factor reducing decay of sandstone monuments in Petra, Jordan. J Cult Herit. 2016;19:415–425.
6. Zammit T, Cassar J. Investigating possible correlations between the porosimetry and insoluble residue content of Malta's Lower Globigerina Limestone. Bull Eng Geol Environ. 2015;76(1):59–70.
7. Stück HL, Platz T, Müller A, Siegesmund S. Natural stones of the Saale–Unstrut Region (Germany): petrography and weathering phenomena. Environ Earth Sci. 2018;77:300.
8. Temraz MG, Khallaf MK. Weathering behavior investigations and treatment of Kom Ombo temple sandstone, Egypt-based on their sedimentological and petrogaphical information. J Afr Earth Sc. 2016;113:194–204.
9. Martínez-Martínez J, Torrero E, Sanz D, Navarro V. Salt crystallization dynamics in indoor environments: Stone weathering in the Muñoz chapel of the cathedral of Santa María (Cuenca, central Spain). J Cult Herit. 2021;47:123–132.
10. Siedel H. Salt efflorescence as indicator for sources of damaging salts on historic buildings and monuments: a statistical approach. Environ Earth Sci. 2018;77(16):572.
11. Sun Q, Dong ZH, Jia HL. Decay of sandstone subjected to a combined action of repeated freezing–thawing and salt crystallization. Bull Eng Geol Environ. 2019;78(8):5951–5964.
12. Gázquez F, Calaforra J-M, Evans NP, Turchyn AV, Rull F, Medina J, Ros A, Llamusí JL, Sánchez J, Hodell DA. Physical weathering of carbonate host-rock by precipitation of soluble salts in caves: a case study in El Orón-Arco Cave (Region of Murcia SE Spain). Chem Geol. 2019;521:1–11.
13. Germinario L, Oguchi CT. Underground salt weathering of heritage stone: lithological and environmental constraints on the formation of sulfate efflorescences and crusts. J Cult Herit. 2021;49:85–93.
14. Roussel E, Vautier F, Voldoire O, André M-F, Cassar J, Fronteau G, Phalip B, Thomachot-Schneider C, Toumazet J-P. Quantifying 450 years of limestone weathering induced by salt crystallization on fortifications in Malta and Gozo. Geomorphology. 2021;378:107614.
15. Yan SJ, Xie N, Liu JH, Li L, Peng LZ, Jiang SW. Salt weathering of sandstone under dehydration and moisture absorption cycles: an experimental study on the sandstone from Dazu rock carvings. Earth Surf Proc Land. 2022;47(4):977–993.
16. Ruedrich J, Siegesmund S. Salt and ice crystallisation in porous sandstones. Environ Geol. 2007;52(2):225–249.
17. Grøntoft T, Cassar J. An assessment of the contribution of air pollution to the weathering of limestone heritage in Malta. Environ Earth Sci. 2020;79(12):288.
18. Marszalek M, Alexandrowicz Z, Rzepa G. Composition of weathering crusts on sandstones from natural outcrops and architectonic elements in an urban environment. Environ Sci Pollut Res. 2014;21(24):14023–14036.
19. Germinario L, Siegesmund S, Maritan L, Simon K, Mazzoli C. Trachyte weathering in the urban built environment related to air quality. Herit Sci. 2017;5:44–60.
20. ICOMOS. Illustrated glossary on stone deterioration patterns. Paris: ICOMOS, Monuments and Sites, XV. 2010.
21. Poppe LJ, Paskevich VF, Hathaway JC, Blackwood DS. A laboratory manual for X-ray powder diffraction. In: US Geological Survey Open File Report 01–041 US Geological Survey, MA. 2002.
22. Ling SX, Wu XY, Zhao SY, Liao XN. Evolution of porosity and clay mineralogy associated with chemical weathering of black shale: a case study of Lower Cambrian black shale in Chongqing, China. J Geochem Explor. 2018;188:326–339.
23. Buczynski C, Chafetz HS. Siliciclastic grain breakage and displacement due to carbonate crystal growth: an example from the Lueders formation (Permian) of north-central Texas, USA. Sedimentology. 1987;34:837–843.
24. Meng Q, Hooker J, Cartwright J. Displacive Widening of Calcite veins in Shale: insights into the force of crystallization. J Sediment Res. 2018;88(3):327–343.
25. Rodriguez-Navarro C, Doehne E. Salt weathering: influence of evaporation rate, supersaturation and crystallization pattern. Earth Surf Proc Land. 1999;24:191–209.
26. Rodriguez-Navarroa C, Doehnea E, Sebastianb E. How does sodium sulfate crystallize? Implications for the decay and testing of building materials. Cem Concr Res. 2000;30:1527–1534.
27. Tsui N, Flatt RJ, Scherer GW. Crystallization damage by sodium sulfate. J Cult Herit. 2003;4(2):109–115.
28. Thaulow N, Sahu S. Mechanism of concrete deterioration due to salt crystallization. Mater Charact. 2004;53:123–127.
29. Zhang XN, Ling SX, Wu XY, Wang FR, Wang J, Teng Q, Xie JW. Hydrochemistry process and microweathering behaviour of sandstone heritages in the Nankan Grotto, China: insights from field micro-observations and water–rock interaction experiments. Bull Eng Geol Environ. 2023;82:356.
30. Elert K, Rodriguez-Navarro C. Degradation and conservation of clay-containing stone: a review. Constr Build Mater. 2022;330:127226.
31. Butscher C, Mutschler T, Blum P. Swelling of Clay-Sulfate Rocks: a review of processes and controls. Rock Mech Rock Eng. 2015;49(4):1533–1549.
32. Sievert T, Wolter A, Singh NB. Hydration of anhydrite of gypsum ($CaSO_4$.II) in a ball mill. Cem Concr Res. 2005;35:623–630.
33. Giustetto R, Pastero L, Aquilano D. Potential effects of the shape of gypsum aggregates on the early sulfation of marble and travertine. J Building Eng. 2020;32:101794.
34. Rees CE, Jenkins WJ, Monster J. The sulphur isotopic composition of ocean water sulphate. Geochim Cosmochim Acta. 1978;42(4):377–381.
35. Li XD, Masuda H, Ono M, Kusakabe M, Yanagisawa F, Zeng HA. Contribution of atmospheric pollutants into groundwater in the northern sichuan basin, China. Geochem J. 2006;40(1):103–119.
36. Wadleigh MA, Blake DM. Tracing sources of atmospheric sulphur using epiphytic lichens. Environ Pollut. 1999;106(3):265–271.
37. Xiao HY, Tang CG, Xiao HW, Liu XY, Liu CQ. Identifying the change in atmospheric sulfur sources in China using isotopic ratios in mosses. J Phys Res. 2009;114:D16304.
38. Li XD, Masuda H, Kusakabe M, Yanagisawa F, Zeng HA. Degradation of groundwater quality due to anthropogenic sulfur and nitrogen contamination in the Sichuan Basin, China. Geochem J. 2006;40(4):309–332.
39. Zheng B, Gao RX. Characteristics of carbon and sulfur isotopes in crude oil and oil-source correlation in the Tarim Basin (in chinese). Petroleum Geol Exp. 2006;28:281–285.
40. Maruyama T, Ohizumi T, Taneoka Y, Minami N, Fukuzaki N, Mukai H, Murano K, Kusakabe M. Sulphur isotope ratios of coals and oils used in China and Japan (in japanese). Chem Soc Japan. 2000;1:45–51.
41. Shen P, Xu YC, Wang JJ, Wang LS. Sulphur isotopic compositions of hydrogen sulphides in natural gases and the sedimentary geochemical facies (in chinese). Acta Sedimentol Sin. 1997;15:216–219.
42. Ruiz-Agudo E, Mees F, Jacobs P, Rodriguez-Navarro C. The role of saline solution properties on porous limestone salt weathering by magnesium and sodium sulfates[J]. Environ Geol. 2007;52(2):269–281.
43. Liu G, Ma L, Liu J. Handbook of chemistry and chemical properties. Beijing: Chemical Industry Press; 2002.

Publisher's Note